Optics Letters

Chirped periodically poled lithium-niobate-on-insulator micro-waveguides for broadband second-harmonic generation

Jiayu Wang,[1] Xiaotian Xue,[1] Jing Qiu,[1] Yongzhi Tang,[1] Rui Ye,[1] Yuting Zhang,[1] Yiwen Huang,[1] Hao Li,[1] Shijie Liu,[1] Yuanlin Zheng,[1,2,4] and Xianfeng Chen[1,2,3,5]

[1]State Key Laboratory of Advanced Optical Communication Systems and Networks, School of Physics and Astronomy, Shanghai Jiao Tong University, Shanghai 200240, China
[2]Shanghai Research Center for Quantum Sciences, Shanghai 201315, China
[3]Collaborative Innovation Center of Light Manipulations and Applications, Shandong Normal University, Jinan 250358, China
[4]ylzheng@sjtu.edu.cn
[5]xfchen@sjtu.edu.cn

Received 21 June 2024; revised 24 August 2024; accepted 27 August 2024; posted 27 August 2024; published 16 September 2024

Periodically poled lithium niobate (LN) waveguides based on quasi-phase matching schemes, benefiting from their high nonlinear coefficient (d_{33}) and strong optical confinement, are widely employed for implementing efficient second-harmonic generation (SHG). Here, we report broadband SHG in z-cut chirped periodically poled lithium-niobate-on-insulator (CPPLNOI) ridge micro-waveguides. Nearly 90-nm-wide SHG at the telecom band is achieved, along with an averaged normalized efficiency of 7.5%/(W·cm^2). We also demonstrate simultaneous generation of second as well as cascaded third and fourth harmonics under direct pumping of femtosecond pulses. This work would benefit applications for frequency conversion of a wideband coherent light source.

https://doi.org/10.1364/OL.533665

Among various optical materials, lithium niobate (LN) has been one of the most attractive and widely used in research and applications, benefiting from its exceptional electro-optic, nonlinear, and acousto-optic properties, as well as its broad transparent window and relatively large refractive index. Compared to the devices on bulk LN, those based on lithium niobate on insulator (LNOI) exhibit higher refractive index contrast and stronger light confinement [1–7], which significantly enhances the light–matter interactions and allows for the miniaturization of integrated photonic devices with superior performance. With the development of wafer-bonding technology and micro-/nano-fabrication, it has received widespread attention as a versatile photonic platform for constructing highly integrated photonic circuits [8–11].

Nonlinear frequency conversion greatly extends the wavelength range of lasers. It has been an essential method to obtain coherent light at different wavelengths, opening up a new stage in the laser technology. Research on frequency conversion has advanced with nonlinear processes, especially second-order ones such as SHG [6], sum-/difference frequency generation (SFG/DFG) [12,13], and optical parametric amplification and oscillation [14]. Efficient wave mixing processes require phase matching, which is a stringent condition due to dispersion. Broadband frequency conversion has raised widespread concern and has a wide range of practical applications, including optical communication and signal processing [15,16], quantum technologies [17–19], and so on. It also holds great potential for various fields, such as spectral analysis [20], atmospheric sounding [21], and biomedicine [22,23]. Achieving phase matching operating in a wide bandwidth while maintaining high conversion efficiency is challenging.

Several schemes have been proposed, to compensate for the phase mismatch in a wide band, such as spectral angular dispersion [24,25], chirped matching [26], and multi-crystal cascade [27]. These schemes are experimentally complicated in both setup and measurement, resulting in inevitable propagation loss and limited bandwidth expansion. In addition, a temperature gradient scheme has been demonstrated to realize broadband birefringence phase matching (BPM) [28]. Nevertheless, this scheme is incapable of utilizing the highest nonlinear coefficient. Compared with these schemes, quasi-phase matching (QPM) schemes based on chirped (or period) domain engineering have notable advantages in flexibility and efficiency. Broadband phase matching is accomplished with abundant reciprocal vectors provided by chirped poling domains [29–32] (or single vector in periodic ones with flat dispersion [33,34]). Meanwhile, as compared to the BPM scheme, the highest nonlinear coefficient is utilized. Furthermore, colinear pumping eliminates the walk-off effect, increasing the nonlinear interaction length.

Here, we demonstrate broadband SHG, spanning 90 nm in telecom bands, in chirped periodically poled micro-waveguides on the 3-μm-thick LNOI platform. In addition, simultaneous second-, cascaded third- and fourth-harmonic generations are also observed under a femtosecond (fs) laser pump. These chirped periodically poled LNOI (CPPLNOI) micro-waveguides enable large-scale and low-cost fabrication while demonstrating efficient fiber-to-fiber performance. It would be beneficial

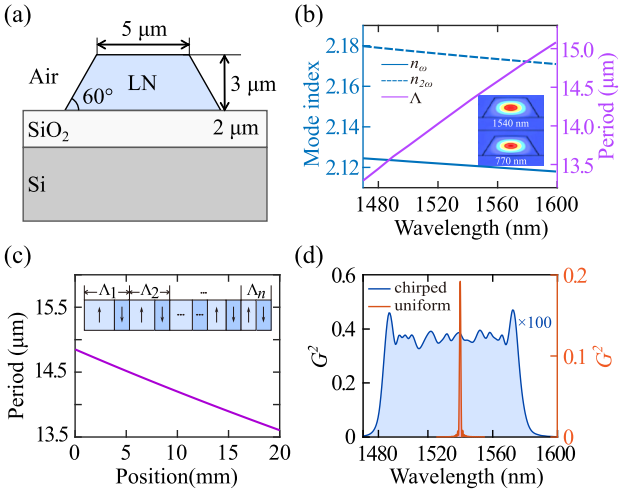

Fig. 1. (a) Schematic of the waveguide end facet and its dimensions. (b) Simulated effective refractive indices of the FH (blue solid) and SH wave (blue dashed), as well as the corresponding QPM poling period (purple). Inset: simulated fundamental TM mode profiles at 1540 and 770 nm. (c) Poling period along the waveguide. Inset: schematic diagram of the chirped poling domains. (d) Calculated G^2 of CPPLNOI (black) and uniform PPLNOI waveguides (orange).

for wide-bandwidth frequency conversion in laser wavelength expansion, signal processing, spectroscopy, quantum technology, etc.

The micro-waveguides are fabricated from a 3-μm-thick LNOI wafer (NANOLN) via UV lithography and deep dry etching procedures. The top layer of the wafer is a 3-μm-thick LN film, bonded on a 2-μm-thick SiO_2 buffer layer on a 500-μm-thick silicon substrate. The wafer is firstly chirped poled according to the first-order QPM conditions, and then the ridge waveguide structure is fabricated. The procedures are the same with that in Ref. [6]. The ridge waveguide on LNOI exhibits strong light confinement and compact modes attributed to the highly refractive index contrast. The type-0 QPM scheme utilizes the highest nonlinear coefficient, d_{33}, of LN. The poling period, Λ, steadily decreases along the propagation direction, y, with a chirp rate of D_g, which is defined as $\Lambda(y) = \Lambda/[1 + (D_g\Lambda y)/2\pi]$. The chirped poling periods provide abundant reciprocal vectors, compensating for the phase mismatch between the SH and FH wave in a broad band, which is the basis for achieving broadband SHG in the CPPLN micro-waveguides.

Figure 1(a) displays the schematic of the micro-waveguide's end facet used in the simulation (consistent with the experimental data), which has a ridge height of 3 μm, a top ridge width of 5 μm, and a sidewall angle of 60°. The simulated effective refractive indices according to the waveguide dimension are shown in Fig. 1(b), representing the fundamental TM modes of the FH and SH wave in the waveguide. The calculated QPM poling period as a function of wavelength is also plotted in Fig. 1(b). The relationship is approximately linear within the wavelength range. Then the calculated chirped period's distribution along the waveguide is obtained, as shown in Fig. 1(c). Starting from the first period $\Lambda_1 = 14.85$ μm at 1580 nm, it steadily decreases to a cutoff period of $\Lambda_n = 13.60$ μm at 1490 nm. The calculated number of poling periods is $n = 1409$ within the 2-cm poling length. The absolute value of the line's slope in Fig. 1(c) corresponds to the chirp rate of the waveguide, i.e., $D_g = 1.94$.

The theoretical normalized conversion efficiency under lossless QPM approximation can be given by [8] $\eta_{\mathrm{SHG}} = \frac{8\pi^2|\Gamma|^2}{c\epsilon_0 n_\omega^2 n_{2\omega}\lambda^2} G^2(\lambda)$, where n is the effective refractive indices of the waveguide mode, ϵ_0 is the vacuum permittivity, λ is the wavelength, and c is the speed of light in vacuum. Γ represents the electric field's overlap factor between the FH and SH wave. $G(\lambda)$ is the amplitude of the Fourier transform of the chirped structure. As shown in the inset in Fig. 1(c), the CPPLNOI waveguide consists of n chirped poling periods, with each period between the coordinates y_{q-1} and y_q (the domain number $q = 1, 2, \ldots, 2n$). A structure function $d(y) = sign(d_{\mathrm{eff}})$ represents the orientation of the poling domain along the propagation direction, taking values of ±1, and $G(\lambda)$ is the Fourier transform of the $d(y)$ function. The expansion of $G^2(\lambda)$ is finally obtained as follows [31]:

$$G^2(\lambda) = \frac{1}{L^2(\Delta k)^2}\left|\sum_{q=1}^{2n} d(y_q)\left(e^{i\Delta k y_q} - e^{i\Delta k y_{q-1}}\right)\right|^2, \quad (1)$$

where L is the length of the QPM grating structure and Δk is the phase mismatch. According to Eq. (1), the calculated G^2 values, representing the theoretical broadband SHG efficiency, are plotted in Fig. 1(d), which corresponds to a CPPLNOI and a uniform PPLNOI waveguide in a length of 2 cm, respectively. The CPPLNOI waveguide dimension is set according to the experimental results (shown later). The uniform QPM grating has a 14.31-μm period for SHG at 1540 nm and a duty cycle of 0.5. The areas of the two efficiency curves are equal, according to the momentum conservation principle. Theoretically, the SH bandwidth of the CPPLN waveguide (~90 nm) is about 45 times wider than that of the uniform PPLN waveguide (~2 nm), and the average efficiency also decreases by roughly 45 times.

Figure 2(a) is an end facet image of the fabricated CPPLNOI micro-waveguide, with a ridge width of 5 μm, a ridge height of 2.97 μm, a sidewall angle of 58°. A closeup view of the poling domains at both ends of the waveguide is shown in Fig. 2(b). The length of the poling period at the left end of the waveguide is around 14.83 μm, while it is roughly 13.61 μm at the right end. The characterization is closely consistent with the theoretical design in Fig. 1(c). The chirp of the QPM period is realized by varying the length of the positive domains, which the negative poling domain is kept to be constant, approximately 7.6 μm.

Firstly, the CPPLNOI micro-waveguide is evaluated for the performance of light coupling efficiency and propagation loss, and the experimental setup is shown in Fig. 2(c). The light source is a tunable continuous-wave (CW) laser (Toptica CTL and DL Pro). A polarization controller (PC) is utilized to adjust the polarization state of the laser. A pair of lens fiber is used to couple light into and out of the waveguide, whose spot size at the focus is comparable to the effective modal area. The output is either spectrally analyzed by an optical spectral analyzer (OSA) or power monitored. A wavelength-division multiplexing (WDM) is employed after the outcoupling fiber, and then two powermeters (PMs) simultaneously measure the output SH and FH power. Light power is measured at the outcoupling fiber port by an optical powermeter. The fiber-to-fiber coupling efficiency is measured to be 45% for the TE input and 40% for the TM input at 1550 nm and both ~25% at 775 nm. The propagation loss of the waveguide, evaluated by the Fabry–Perot (FP) interferometric method, is approximately 0.5 dB/cm at 1550 nm for TE mode (corresponding to the ee-e

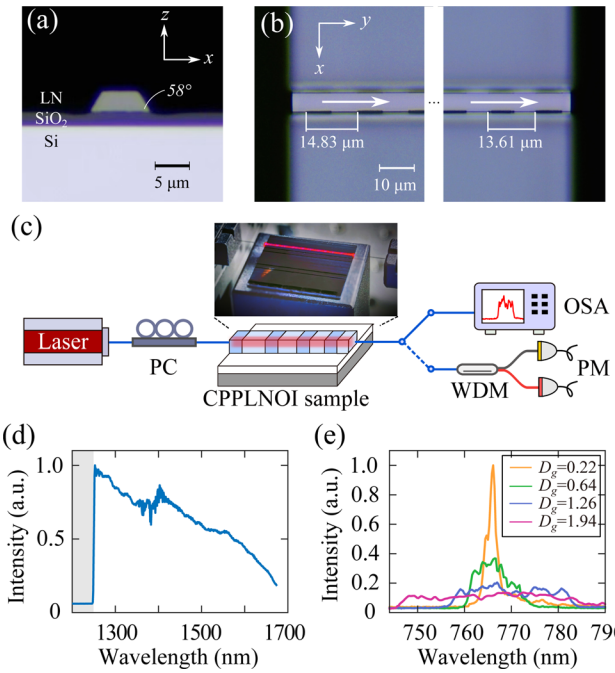

Fig. 2. (a) Cross section of the waveguide end facet. (b) Top view of poled domains at waveguide ends. (c) SHG experiment setup. Inset: SHG in the waveguide. (d) Spectrum of the filtered SCG pump. (e) Measured normalized SHG spectra of four CPPLNOI micro-waveguide samples using the SCG pump.

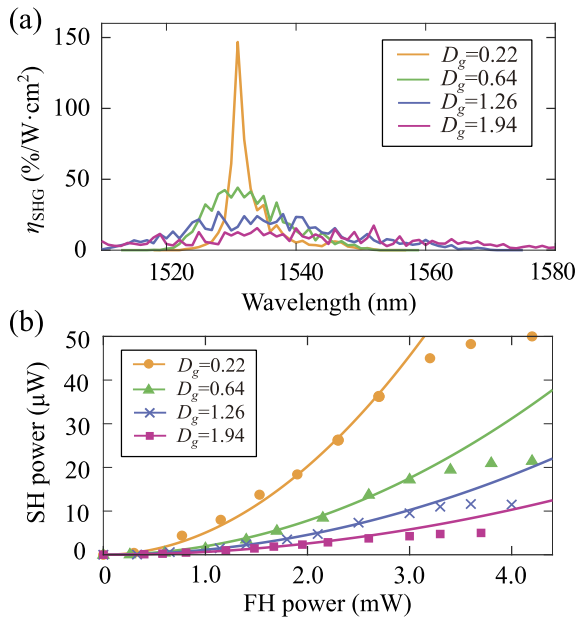

Fig. 3. (a) Measured normalized broadband SHG spectra using the CW pump. (b) Quadratic power dependence of the SH wave on FH.

QPM). Thus, the fiber–waveguide coupling loss is estimated to be around 1.2 dB/facet without antireflection coating. Overall, the micro-waveguide indicates low light propagation and coupling loss in the experiment, demonstrating the advanced micro-scale fabrication of device on the 3-μm-thick LNOI platform.

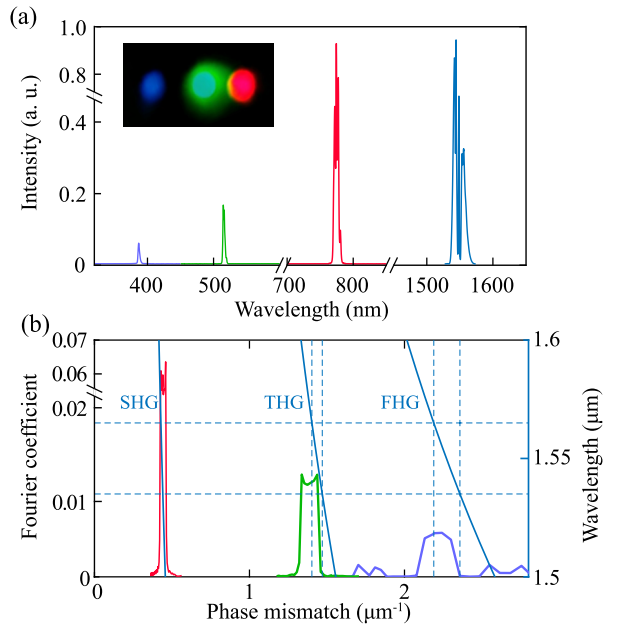

Fig. 4. (a) Measured spectra of the input fs laser and cascaded harmonic generation in the CPPLNOI micro-waveguide (D_g = 1.94). Intensity not to scale. Inset: generated harmonic light spots after being dispersed by a prism. (b) Plots of calculated dispersion and RLV curves.

Then, broadband SHG performance of the CPPLNOI micro-waveguides is investigated using a supercontinuum laser. The wideband FH pump used in this experiment is a supercontinuum generation (SCG) source (range 430–2400 nm) filtered by a 1250-nm long-pass filter, whose spectrum is displayed in Fig. 2(d). The seed inside the supercontinuum laser is a high-power 1060-nm picosecond pulsed laser with a repetition rate of 200 MHz. As shown in the inset of Fig. 2(c), the generated SH wave in the waveguide is obvious. The generated SH spectra are recorded by an optical spectrum analyzer (OSA), and the normalized results are shown in Fig. 2(e). The chirp rates and the corresponding SH spectral range are 1). D_g = 0.22, 764–769 nm (5 nm wide), 2). D_g = 0.64, 760–775 nm (15 nm wide), 3). D_g = 1.26, 755–785 nm (30 nm wide), and 4). D_g = 1.94, 745–790 nm (45 nm wide), respectively. The results agree well with the theoretical prediction. The CPPLNOI micro-waveguides demonstrate effective broadband spectra with a SHG bandwidths of approximately 10, 30, 60, and 90 nm in the telecom bands.

To be more precise, the broadband SHG efficiency curves are further confirmed using the CW pump. Figure 3(a) displays the measured broadband SHG efficiency, corresponding to the chirp rates and broadband ranges of 1). D_g = 0.22, 1528–1538 nm (10 nm wide), 2). D_g = 0.64, 1520–1550 nm (30 nm wide), 3). D_g = 1.26, 1510–1570 nm (60 nm wide), and 4). D_g = 1.94, 1510–1580 nm (width limited by the laser). The CPPLNOI micro-waveguide samples are tested in the full wavelength tunable range of the CW laser. Broadband SHG of approximately 10, 30, 60, and >70 nm is obtained, consistent with the SHG spectra under the SCG pump shown in Fig. 2(e). According to the spectrum, the CPPLNOI waveguide with D_g = 1.94 exhibits the potential for SHG across a bandwidth of approximately 90 nm with an averaged normalized efficiency of 7.5%/(W·cm^2), and the highest efficiency reaches up to 17%/(W·cm^2) at 1552 nm.

The result is on par with the state-of-the-art result demonstrated in thin-film lithium niobate nanowaveguides [31]. An effective broadband SHG is observed in the $D_g = 1.26$ waveguide across a 60-nm wavelength range, with a maximum normalized efficiency of 27%/(W·cm^2) at 1528 nm. For the waveguides with lower chirp rates ($D_g = 0.22, 0.64$), the observed SHG bandwidth is less than 30 nm, but the maximum normalized efficiency is around 150%/(W·cm^2). The 90-nm-width normalized SHG efficiency curve exhibits more fluctuations compared to the theoretical G^2 function shown in Fig. 1(d). The reason may be that the coupling and propagation loss for FH and SH is not constant in the broadband range. As shown in Fig. 3(b), the quadratic power dependency between the FH and SH waves under small-signal approximation condition is confirmed in all the four CPPLNOI waveguides. The measured FH wavelengths for each waveguide are 1531, 1531, 1528, and 1552 nm, respectively, at which the waveguides display their highest normalized SHG efficiency.

In addition, cascaded harmonic generation is observed using the fs laser pump. The mode-locked fs pulsed laser employed in the experiment delivers 500-fs pulses centered at ~1551 nm with a repetition rate of 80 MHz. The coupled pump power is approximately 10 mW, i.e., 0.125 nJ/pulse. The generated light is collimated using an objective lens and then dispersed by a prism. Red, green, and blue–violet spots corresponding to the SH, third harmonic (TH), and fourth harmonic (FH) are dispersed and projected on a screen. The spectra of the fs laser and the generated light are plotted in Fig. 4(a), which range from 1530 to 1570 nm, 768 to 782 nm, 512 to 521 nm, and 384 to 391 nm, respectively. TH and FH correspond to the SHG and the subsequent cascaded SFG. Figure 4(b) shows combined plots of dispersion and reciprocal lattice vector (RLV) curves, illustrating the mechanisms of SHG and cascaded SFG in the CPPLNOI structure. The intersection points on the dotted lines of the y axis (right side) and x axis show that the QPM condition is fulfilled in the range of the input pulsed laser. The observed cascading processes infer that the broadband QPM as well as the group velocity matching in the waveguide is well satisfied, showing the capability of our micro-waveguide in achieving broadband and efficient frequency conversion.

In conclusion, we have demonstrated broadband SHG in the CPPLNOI micro-waveguide on the 3-μm-thick LNOI platform, showing a bandwidth of around 90 nm in the telecom bands. On the basis of the observed simultaneous SH, cascaded TH and FH generation is also obtained. Overall, this study is beneficial for the broadband nonlinear frequency conversion of both CW and pulsed light sources.

Funding. National Key Research and Development Program of China (2022YFA1205101, 2023YFA1407202); National Natural Science Foundation of China (12074252, 12192252); Shanghai Municipal Science and Technology Major Project (2019SHZDZX01-ZX06); Yangyang Development Fund.

Disclosures. The authors declare no conflicts of interest.

Data availability. Data underlying the results presented in this paper are not publicly available at this time but may be obtained from the authors upon reasonable request.

REFERENCES

1. A. Boes, B. Corcoran, L. Chang, *et al.*, Laser Photonics Rev. **12**, 1700256 (2018).
2. A. Honardoost, K. Abdelsalam, and S. Fathpour, Laser Photonics Rev. **14**, 2000088 (2020).
3. J. Lin, F. Bo, Y. Cheng, *et al.*, Photonics Res. **8**, 1910 (2020).
4. D. Zhu, L. Shao, M. Yu, *et al.*, Adv. Opt. Photonics **13**, 242 (2021).
5. G. Chen, N. Li, J. D. Ng, *et al.*, Adv. Photonics **4**, 034003 (2022).
6. Y. Zhang, H. Li, T. Ding, *et al.*, Optica **10**, 688 (2023).
7. A. Boes, L. Chang, C. Langrock, *et al.*, Science **379**, eabj4396 (2023).
8. C. Wang, C. Langrock, A. Marandi, *et al.*, Optica **5**, 1438 (2018).
9. J. Lu, J. B. Surya, X. Liu, *et al.*, Optica **6**, 1455 (2019).
10. J. Lu, A. A. Sayem, Z. Gong, *et al.*, Optica **8**, 539 (2021).
11. C. Lu, H. Li, J. Qiu, *et al.*, Opt. Express **30**, 1381 (2022).
12. X. Ye, S. Liu, Y. Chen, *et al.*, Opt. Lett. **45**, 523 (2020).
13. Y. Niu, C. Lin, X. Liu, *et al.*, Appl. Phys. Lett. **116**, 101104 (2020).
14. A. W. Bruch, X. Liu, J. B. Surya, *et al.*, Optica **6**, 1361 (2019).
15. M. Pu, H. Hu, L. Ottaviano, *et al.*, Laser Photonics Rev. **12**, 1800111 (2018).
16. D. Kong, Y. Liu, Z. Ren, *et al.*, Nat. Commun. **13**, 4139 (2022).
17. U. A. Javid, J. Ling, J. Staffa, *et al.*, Phys. Rev. Lett. **127**, 183601 (2021).
18. Y. Huang, J. Feng, Y. Li, *et al.*, Phys. Rev. Appl. **17**, 054002 (2022).
19. N. Namekata, N. Kobayashi, K. Nomura, *et al.*, Sci. Rep. **13**, 21080 (2023).
20. N. Nader, D. L. Maser, F. C. Cruz, *et al.*, APL Photonics **3**, 036102 (2018).
21. B. J. Bjork, T. Q. Bui, O. H. Heckl, *et al.*, Science **354**, 444 (2016).
22. S. Moon and D. Y. Kim, Opt. Express **14**, 11575 (2006).
23. S. Rao DS, M. Jensen, L. Grüner-Nielsen, *et al.*, Light: Sci. Appl. **10**, 133 (2021).
24. P. Baum, S. Lochbrunner, and E. Riedle, Opt. Lett. **29**, 1686 (2004).
25. J. P. Torres, M. Hendrych, and A. Valencia, Adv. Opt. Photonics **2**, 319 (2010).
26. C. Vicario, A. Trisorio, G. Arisholm, *et al.*, Opt. Lett. **37**, 1619 (2012).
27. X. Feng, J. Shi, P. Liu, *et al.*, Opt. Express **28**, 14310 (2020).
28. Y. Tang, T. Ding, C. Lu, *et al.*, Opt. Lett. **48**, 1108 (2023).
29. B.-Q. Chen, M.-L. Ren, R.-J. Liu, *et al.*, Light: Sci. Appl. **3**, e189 (2014).
30. D. D. Hickstein, D. R. Carlson, A. Kowligy, *et al.*, Optica **4**, 1538 (2017).
31. X. Wu, L. Zhang, Z. Hao, *et al.*, Opt. Lett. **47**, 1574 (2022).
32. T.-H. Wu, L. Ledezma, C. Fredrick, *et al.*, Nat. Photonics **18**, 218 (2024).
33. G. Li, Y. Chen, H. Jiang, *et al.*, Opt. Lett. **42**, 939 (2017).
34. L. Ge, Y. Chen, H. Jiang, *et al.*, Photonics Res. **6**, 954 (2018).